Supporting Information

3D Structure-Functional Design of Biomass-derived Photocatalyst for Antimicrobial Efficacy and Chemical Degradation at Ambient Conditions

Wan Zhang,[a,b] Yuanhao Liang,[a,b] Cheng Hu,[a,b] Weiwei Li,[c] Jingru Lai,[a,b] Kainan Chen,[a,b] Sisi Xiang,[d] Dariusz Niedzwiedzki,[f] Jing Wu,[d] Andrew Li,[e] Susie Y. Dai *[a,b,g]

[a]Department of Plant Pathology and Microbiology, Texas A&M University, College Station, TX 77843
[b]Systems and Synthetic Biology Innovation Hub, Texas A&M University, College Station, TX 77843
[c] Department of Energy, Environmental, and Chemical Engineering, Washington University in St. Louis, St. Louis, MO 63130, USA
[d]Materials Characterization Facility, Texas A&M University, College Station, TX 77843, USA
[e]Department of Chemical Engineering, Texas A&M University, College Station, TX 77843
[f]Center for Solar Energy and Energy Storage and Department of Energy, Environmental and Chemical Engineering, Washington University in St. Louis St. Louis, MO 63130 USA
[g]Department of Civil and Environmental Engineering, Texas A&M University, College Station, TX

Corresponding author: Susie Y. Dai, sydai@tamu.edu

Table of Contents

1. Characterization

To examine the presence of chemical functional groups, fourier transform infrared spectroscopy (FTIR) were generated using Thermo Nicolet 380 FTIR spectrometer in the wavelength range from 400 to 4000 cm^{-1}. Chemical element and chemical bonding were examined based on the X-Ray photoelectron spectroscopy (XPS) spectra developed using Omicron XPS/UPS system with Argus detector and the Omicron's DAR 400 dual Mg/Al X-ray source (Mg, power of 300 W, SCR_022202). Scanning electron microscopy (SEM) images were recorded on an ultra-high resolution field emission scanning electron microscope (JEOL JSM-7500F, SCR_022202) equipped with a high brightness conical FE gun and a low aberration conical objective lens at an accelerating voltage of 5 kV. Transmission Electron Microscopy (TEM) and Energy-Dispersive X-ray Spectroscopy (EDS) were used to analyze the samples by using the Titan Themis 300 microscopes (SCR_022202). The samples were prepared by dispersing the dry powders of the nanoparticles in ethanol through ultrasonication for one min. The dispersion of each sample was deposited dropwise on the 400 mesh copper grids with an ultrathin carbon film of lacey carbon and dried in an open atmosphere. Particle sizes were investigated with a Malvern DLS zeta potential analyzer at ambient temperature using ethanol as the solvent. All data were averaged over 6 cycles with 10 scans for each cycle. UV-vis diffuse reflectance spectra (UV-vis ERS) were measured on a Hitachi U4100 UV-vis–NIR spectrophotometer (Japan) with a Praying Mantis accessory. Thermogravimetric analysis (TGA) test was performed on a TGA 5500 thermogravimetric analyzer. About 5.0 mg of sample was heated from room temperature to 800 °C at a heating rate of 10 °C/min under the N_2 atmosphere. All data were processed with software Origin 2022. EPR were texted with Bruker Elexsys E500 console with a standard resonator and CoolEdge cryo system.

Band energy calculation

The band gap energy (Eg) was calculated from the UV–vis spectrum using the Tauc Plot method, by analyzing the linear relationship between $(\alpha h\upsilon)^{1/2}$ and photon energy $h\upsilon$.[1] In these plots, the Eg values were obtained from the intercept of the extrapolation of the linear branch with the abscissa.

Quantitative PFAS and atenolol analysis by high-pressure liquid chromatography-mass spectrometry (LCMS).

Filtered PFAS or atenolol sample solutions (10μL) were loaded into a 3.0 mm × 50 mm (1.7 μm) Acquity UPLC BEH C18 column (Waters, MA, USA) to separate the compounds. An ammonium acetate aqueous solution (20 mM, solvent A) and 100% methanol (solvent B) were used as mobile phases, with a flow rate of 300 μL/min. The LC gradient started with 95% solvent A and 5% solvent B, and this ratio was kept until 1.00 min, then increased solvent B to 100% until 6.00 min, and kept the ratio until 7.00 min. Subsequently, the ratio was changed to 5% solvent B and 95% solvent A until 15.00 min. The mass spectrometer TSQ Quantiva (Thermo Fisher Scientific, San Jose, CA) was operated with a high temperature ESI source in negative mode. For PFAS, the ion source related parameters were: spray voltage: static; negative ion: 3219 V; sheath gas: 38.3 Arb; aux gas: 1.2 Arb; sweep gas: 2.8 Arb; Ion transfer tube

temp: 325 °C; vaporizer temp: 50 °C; CID gas: 1.5 m Torr. For atenolol, the ion source related parameters were: spray voltage: static; positive ion: 4281 V; sheath gas: 38.3 Arb; aux gas: 1.2 Arb; sweep gas: 2.8 Arb; Ion transfer tube temp: 325 °C; vaporizer temp: 50 °C; CID gas: 1.5 mTorr. The calibration solutions were diluted with water to the corresponding concentration. Both calibration solutions and samples included internal standards with a spiked concentration of 5 μg/L.

Antibacterial performance in solution

Pseudomonas putida A514 was inoculated in LB media with OD 600 of 0.2, and then the *Pseudomonas putida* solution was diluted into 1×10^{-5}. Each 2 mL of the above solution was put into sealed clear glass bottles with 30 mg, 45 mg and 60 mg C_{lignin}@H-TiO_2, respectively. Then the 3 samples were put under a plant growth light (XS2000 LED Grow Light, 200 W, Viparspectra) for 1 h. Afterwards, 200 uL of the light treated *Pseudomonas putida* solutions were taken out and evenly distributed onto Luria-Bertani agar plates supplemented with ampicillin (LB^{Amp}). The agar plates were then incubated at 30°C overnight, allowing for the growth of bacterial colonies. As a reference, control samples of *Pseudomonas putida* solutions with and without light were also tested.

Steady-state fluorescence

Steady-state photoluminescence emission and excitation spectra were recorded using RF-6001 fluorometer from Shimadzu. The films deposited on quartz slides were positioned at 45 degree in respect to excitation/emission slits. The widths of excitation and detection slits were set to 5 nm. To minimize effect of reflected and scattered light, 375 nm long-pass filter was placed at the detection entrance. All experiments were performed at room temperature in ambient air atmosphere.

Transient absorption

Time-resolved pump-probe absorption (transient absorption) experiments were carried out using Helios-EOS, a femtosecond/nanosecond tandem transient absorption spectrometer (Ultrafast Systems, USA) coupled to a femtosecond laser system (Spectra-Physics, USA), consisting Solstice, a one box ultrafast amplifier (Spitfire Pro XP - a Ti:sapphire regenerative amplifier with a pulse stretcher and compressor, Mai-Tai, a femtosecond oscillator and Empower, a diode-pumped solid state pulsed green laser). The laser system generates pulses at 800 nm with energy of ~3.5 mJ, 1 kHz repetition rate and ~90 fs duration. The output beam was split to 90 and 10%. Pump beam generated from 90% split was done by Topas Prime, an optical parametric amplifier (Light Conversion Ltd, Lithuania). The remaining 10% is used to produce probe pulses in the Helios spectrometer. For measurements in the EOS spectrometer (μs-ms delay time-range), probe pulses (~1 ns duration) are generated by built-in PCF based supercontinuum pulsed light source. All samples were excited at 350 nm with energy of 1 μJ with excitation beam focused to 1 mm circular spot (2.3×10^{14} photons/cm^2, ~0.1 J/cm^{-2} fluence). To provide an isotropic excitation of the sample and avoid pump-probe polarization effects the pump beam was depolarized with achromatic depolarizer (DPU-25, Thorlabs). All experiments were performed at room temperature in ambient air atmosphere.

Data processing and analysis of transient absorption datasets

TA datasets were globally fitted with a kinetic model assuming (if more than one spectro-kinetic component was present) irreversible sequential decay of photoexcited species in slower steps, giving the so-called evolution associated difference spectra (EADS). According to this model, the TA signal at any time delay *t,* and wavelength λ, $\Delta A(t,\lambda)$, is reconstructed from the superposition of the n^{th} $C_i(t)$ and $EADS_i(\lambda)$ products according to the formula:

$$\Delta A(t,\lambda) = \sum_{i=1}^{n} C_i(t)\, EADS_i(\lambda) \quad (1)$$

where $C_i\,(t)$ is the time-dependent concentration of the i^{th} EADS defined as:

$$\frac{dC_i(t)}{dt} = k_{i-1}C_{i-1}(t) - k_iC_i(t),\ i \neq 1, k_{i-1} > k_i \quad (2)$$

k_i is the rate constant of $EADS_i$, and $C_{i=1}(t)$ is populated by the excitation pulse represented by the instrument response function, IRF:

$$\frac{dC_1(t)}{dt} = IRF - k_1C_1(t) \quad (3)$$

For fitting purposes, the IRF was simulated by a Gaussian with a full width at half maximum (FWHM) of ~800 ns. The kinetic analysis was done using CarpetView software (Light Conversion Ltd., Lithuania).

Photocurrent and electrochemical impedance spectroscopy

Fluorine tin oxide (FTO) glass was employed as the transparent conductive substrate for the working electrode, which was cleaned by sonication in acetone, isopropanol, and water sequentially, followed by being blown with nitrogen gas to dry before use. Samples were suspended in ethanol by sonicating for 1h to produce a solution, which were then spray-coated onto an FTO glass and dried before test. The Photoelectric analysis was performed on a Bio-Logic SP 150e potentialstat utilizing a three-electrode photoelectrochemical cell with the FTO glass, a Pt wire, and an Ag/AgCl electrode as the working, counter and reference electrodes, respectively, in an aqueous electrolyte of 0.5 M Na_2SO_4. The area of the sample on the FTO exposed to light was 1cm^2. The EIS measurements were performed over a range from 0.01 to 100 kHz at 0 V versus OCP, and the amplitude of the applied potential in each case was 10 mV.

2. Particle Size Analysis

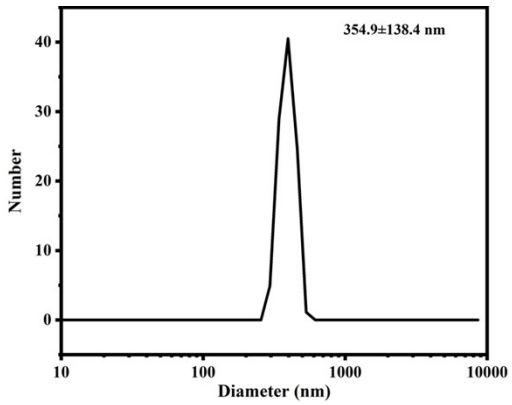

Fig. S1 Particle size analysis of C_{lignin}@H-TiO_2.

3. The Lattice Fringes and the Crystal Pattern of C_{lignin}@H-TiO_2

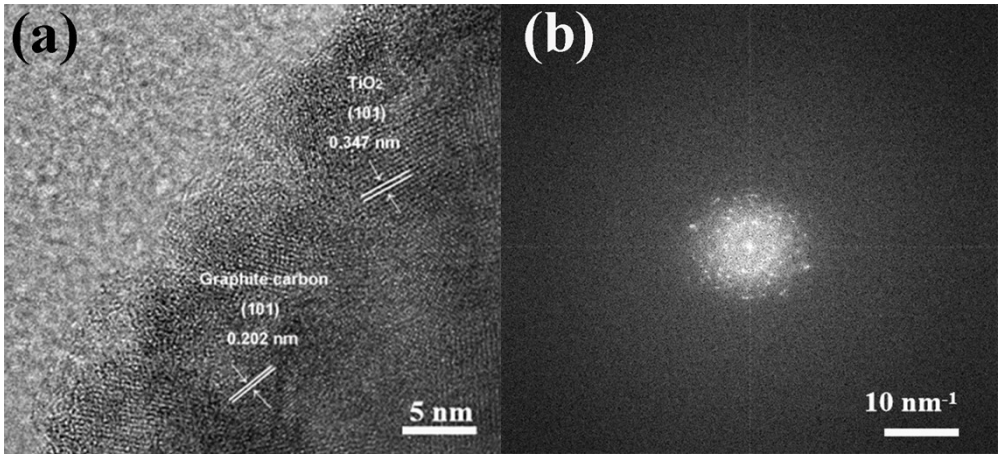

Fig. S2 (a) The lattice fringes and (b) the crystal pattern of C_{lignin}@H-TiO_2.

4. Effect of Crystal Type of C_{lignin}@H-TiO_2 on Atenolol Degradation

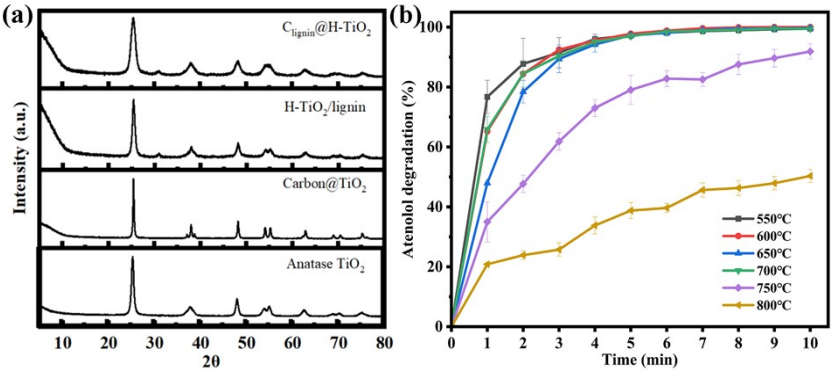

Fig. S3 (a) XRD patterns of C_{lignin}@H-TiO_2; (b) Atenolol degradation performance by the C_{lignin}@H-TiO_2 materials synthesized at varying temperatures.

5. Controllable Particle Structure of C_{lignin}@H-TiO_2

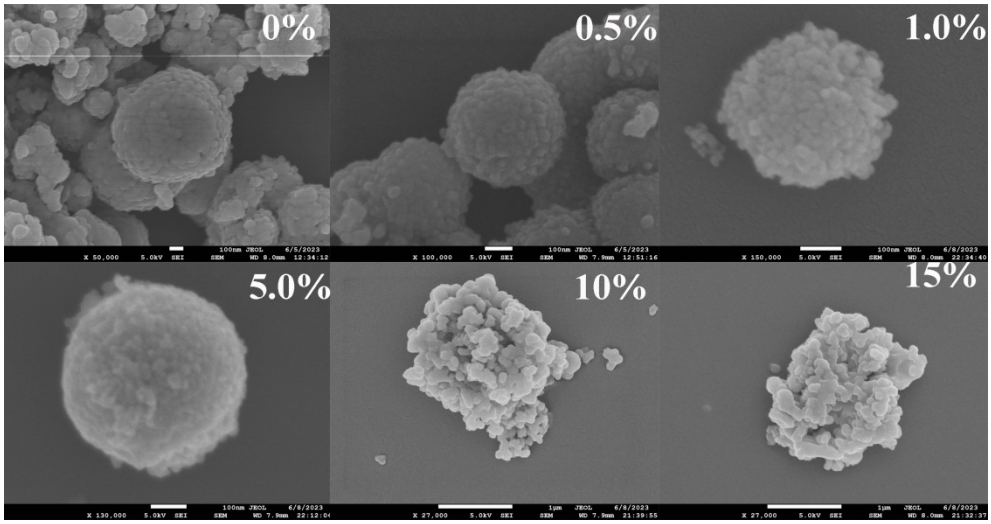

Fig. S4 Morphology of C_{lignin}@H-TiO_2 synthesized with different percentage lignin.

6. Electrical Conductivity

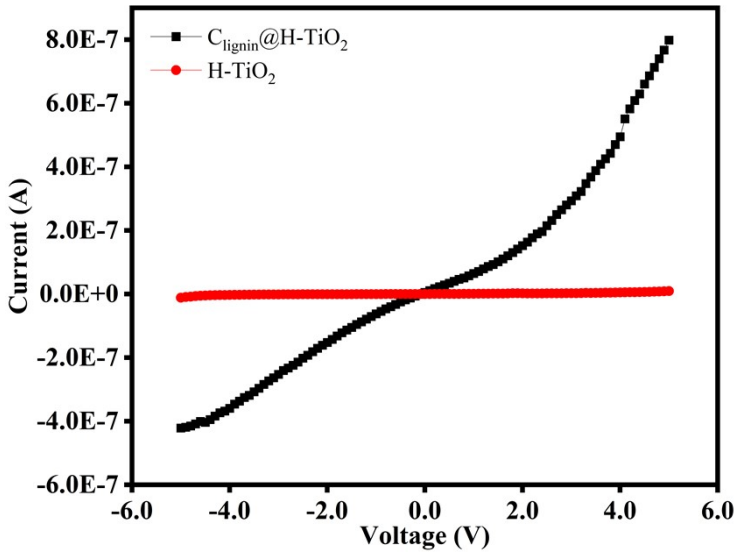

Fig. S5 Electrical conductivity of C_{lignin}@TiO_2 and H-TiO_2.

7. Effect of C_{lignin} on the Crystalline Structures of C_{lignin}@H-TiO_2

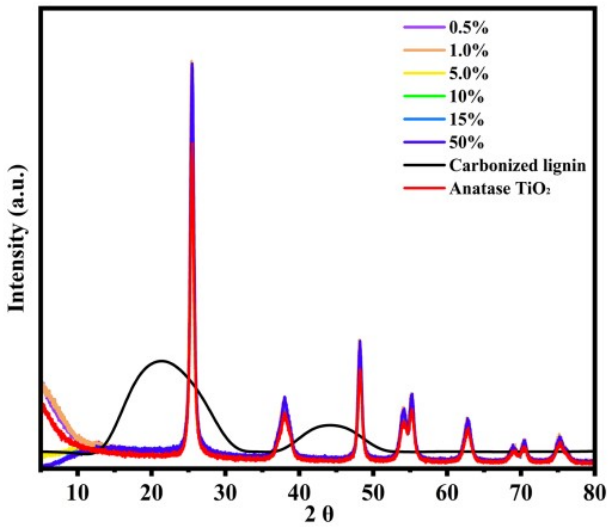

Fig. S6 XRD patterns of C_{lignin}@H-TiO_2 materials synthesized with different lignin content at 600°C for 90 min.

8. DMPO Spin-trapping ESR Spectra

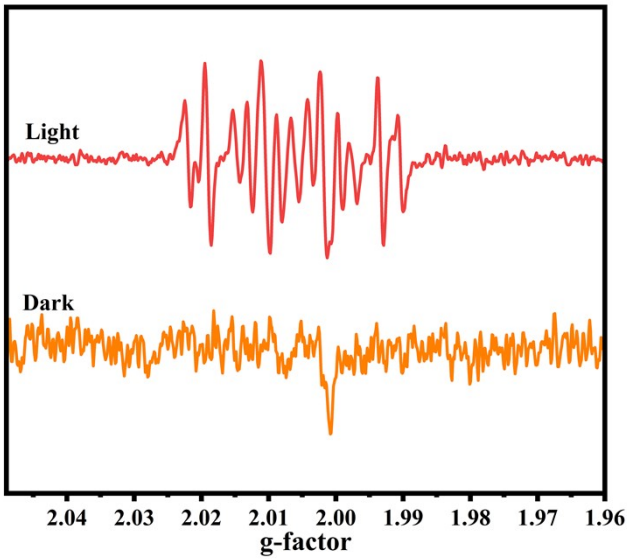

Fig.S7 DMPO spin-trapping ESR spectra of C_{lignin}@H-TiO_2 with solar light (red line) and C_{lignin}@H-TiO_2(orange line) in dark.

9. Electrochemical impedance, photocurrent response and photoluminescence measurements

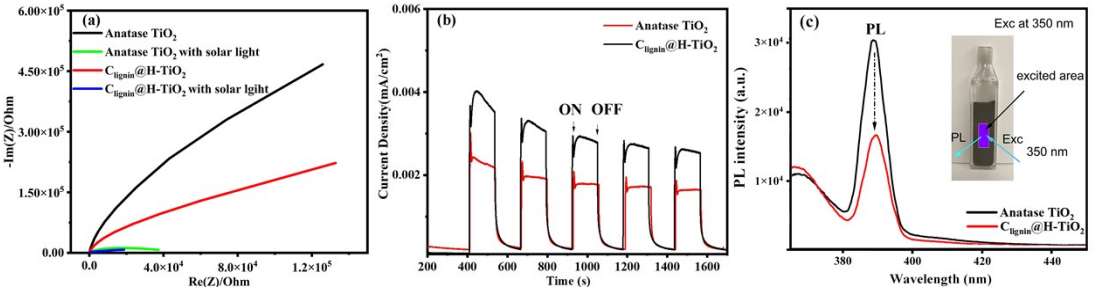

Fig. S8 (a) Electrochemical impedance of anatase TiO_2, anatase TiO_2 with solar light, C_{lignin}@H-TiO_2 and C_{lignin}@H-TiO_2 with solar light; (b) Photocurrent response of anatase TiO_2 and C_{lignin}@H-TiO_2; (c) Steady-state photoluminescence emission (PL) spectra of anatase TiO_2 and C_{lignin}@H-TiO_2 after excitation (Exc) at 350 nm.

10. Antibacterial Properties of C_{lignin}@H-TiO_2

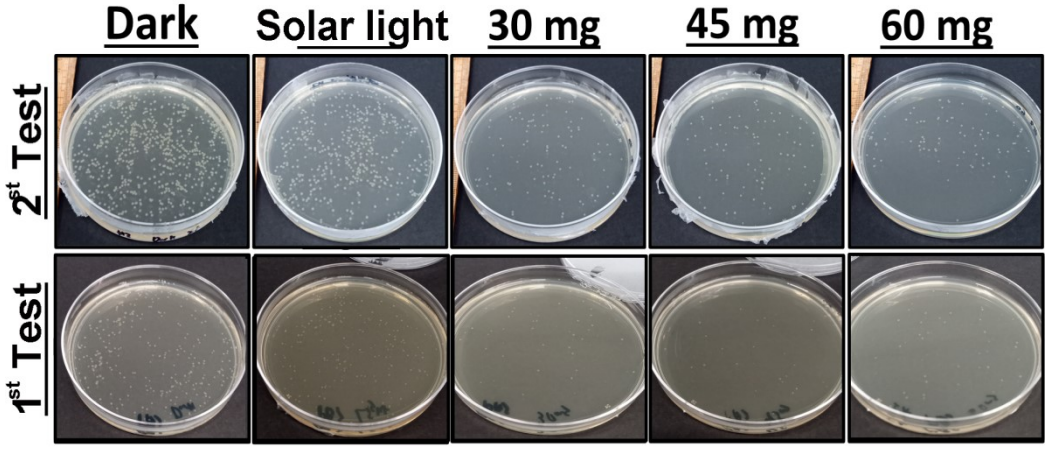

Fig. S9 Antibacterial performance of C_{lignin}@H-TiO_2. The bacterial treatment was repeated twice.

11. Atenolol Degradation Performance with TiO_2 based Photocatalytic Materials

Table S1 Atenolol degradation performance of TiO_2 based photocatalytic materials

Catalytic material	Light source	Degradation time	Degradation rate	Degradation environmental solvent	Reference
TiO_2 (degussa P25)	9 W UVA lamp	30 min	67 %	Ultrapure water	2
Carbon dot/TiO_2 composite	1000 W Xenon lamp	180 min	89%	Water	3
Alginate supported TiO_2 nanoparticles	UVA tube having 365 nm wavelengths	60 min	58%	Water, pH 10.5	4
Slurry suspension of TiO_2 (degussa P25)	UV radiometer of 30 W m^{-2}	33.4 min	100 %	Water	5
TiO_2 (degussa P25)	1000 W Xe-OP lamp	120 min	63%	Ultrapure water	6
Graphene oxide-TiO_2 composite	1000 W Xe arc lamp and an AM 1.5G filter	60 min	72%	Deionized water	7
Heterojunction S-Tyr-	300 W Xenon	120 min	95.46%	Deionized	8

NDI-Tyr/TiO_2	lamp equipped with a 420 nm filter			water	
TiO_2 (degussa P25)	High pressure Mercury lamp (Philips, HPK, 125 W)	60 min	100%	Milli-Q water	9
Aeroxide® TiO_2 P25	UVA radiation, 28 W m^2	75min	100%	Distilled water	10
C_{lignin}@H-TiO_2	Solar simulator with 1800 W/m^2 Xenon lamp	5 min	100%	Deionized water	This research

12. Sterilization Performance of C_{lignin}@H-TiO_2 Coating

Table S2 Sterilization performance of C_{lignin}@H-TiO_2 coating

Samples		Bacterial colonies/ number
With light	C_{lignin}@H-TiO_2 coated area	48
	Disinfecting wipe wiped area	49
	Uncoated and unwiped areas	82
Without light	C_{lignin}@H-TiO_2 coated area	190
	Disinfecting wipe wiped area	180
	Uncoated and unwiped areas	236

References

1. Makuła, P., Pacia, M., and Macyk, W. (2018). How to correctly determine the band gap energy of modified semiconductor photocatalysts based on UV–Vis spectra. J. Phys. Chem. Lett. 9, 6814-6817. https://doi.org/10.1021/acs.jpclett.8b02892
2. Hapeshi, E., Achilleos, A., Vasquez, M.I., Michael, C., Xekoukoulotakis, N.P., Mantzavinos, D., and Kassinos, D. (2010). Drugs degrading photocatalytically: kinetics and mechanisms of ofloxacin and atenolol removal on titania suspensions. Water Res. 44, 1737-1746. https://doi.org/10.1016/j.watres.2009.11.044
3. Ponkshe, A., and Thakur, P. (2022). Solar light–driven photocatalytic degradation and mineralization of beta blockers propranolol and atenolol by carbon dot/TiO2 composite. Environ Sci. Pollut. Res. 29, 15614–15630. https://doi.org/10.1007/s11356-021-16796-w
4. Sarkar, S., Chakraborty, S., and Bhattacharjee, C. (2015). Photocatalytic degradation of pharmaceutical wastes by alginate supported TiO2 nanoparticles in packed bed photo reactor (PBPR). Ecotoxicol. Environ. Saf. 121, 263-270. https://doi.org/10.1016/j.ecoenv.2015.02.035
5. Radjenović, J., Sirtori, C., Petrović, M., Barceló, D., and Malato, S. (2009). Solar photocatalytic degradation of persistent pharmaceuticals at pilot-scale: kinetics and characterization of major intermediate products. Appl. Catal., B 89, 255-264. https://doi.org/10.1016/j.apcatb.2009.02.013
6. Ioannou, L., Hapeshi, E., Vasquez, M., Mantzavinos, D., and Fatta-Kassinos, D. (2011). Solar/TiO2 photocatalytic decomposition of β-blockers atenolol and propranolol in water and wastewater. Sol. Energy 85, 1915-1926. https://doi.org/10.1016/j.solener.2011.04.031
7. Bhatia, V., Malekshoar, G., Dhir, A., and Ray, A.K. (2017). Enhanced photocatalytic degradation of atenolol using graphene TiO2 composite. J. Photochem. Photobiol., A 332, 182-187. https://doi.org/10.1016/j.jphotochem.2016.08.029
8. Liu, D., Chen, Y., Guan, R., Zhao, J., Jin, H., Zhang, S., and Shang, Q. (2022). Photocatalytic performance of heterojunction S-Tyr-NDI-Tyr/TiO2 formed by self-assembled naphthalimide derivatives and titanium dioxide. Chemosphere 296, 134046. https://doi.org/10.1016/j.chemosphere.2022.134046
9. Ji, Y., Zhou, L., Ferronato, C., Yang, X., Salvador, A., Zeng, C., and Chovelon, J.-M. (2013). Photocatalytic degradation of atenolol in aqueous titanium dioxide suspensions: kinetics, intermediates and degradation pathways. J. Photochem. Photobiol., A 254, 35-44. https://doi.org/10.1016/j.jphotochem.2013.01.003
10. Marquez, G., Rodriguez, E.M., Maldonado, M.I., and Alvarez, P.M. (2014). Integration of ozone and solar TiO2-photocatalytic oxidation for the degradation of selected pharmaceutical compounds in water and wastewater. Sep. Purif. Technol. 136, 18-26.